Supporting Information:

Oxygen absorption and influence on the thermoelectric performance of polycrystalline SnSe

Mengmeng Zhang,[⊥] Dongyang Wang,[⊥] Cheng Chang,[⊥,*] Tao Lin,[#] Kedong Wang,[#] Li-Dong Zhao[⊥,*]

[⊥]School of Materials Science and Engineering, Beihang University, Beijing 100191, China

[#]Department of Physics, South University of Science and Technology, Shenzhen 518055, China

KEYWORDS: thermoelectrics, SnSe, oxygen absorption, electrical transport, electronegativity

Materials and Methods

Starting materials: Sn shot (99.999%, Aladdin, China), Se shot (99.999%, Aladdin, China), Te shot (99.999%, Aladdin, China), S shot (99.999%, Aladdin, China) and $SnBr_2$ powder (99.2%, Alfa, US).

Synthesis: To prepare the polycrystals (~ 12g) with nominal compositions of $SnSe_{1-x}Br_x$ (x=0-0.04), high-purity elements were loaded into quartz tubes with stoichiometric ratios in an N_2-filled glove box. All tubes were flame-sealed under a vacuum of 10^{-3} Torr, then placed them into another bigger quartz tubes to prevent from oxidation in case the inner tubes break when cooling to room temperature due to the difference of thermal expansion between the ingots and the quartz. The sealed quartz tubes were slowly heated to 1223 K within 10h and maintained for 10 h, then cooled to room temperature in the furnace. The obtained ingots were ground into powders inside and outside the glove box respectively to regulate the existence of oxygen, and sintered by spark plasma sintering (SPS-211Lx) at 793 K for 5 min in a Φ 12.7 mm graphite die under an axial pressure of 50 MPa in vacuum. The densified cylinder-shaped samples were obtained, which were used for subsequent thermoelectric transport properties measurement. The polycrystals with nominal compositions of $SnSe_{0.97-x}S_xBr_{0.03}$ and $SnSe_{0.97-x}Te_xBr_{0.03}$ (x=0.05-0.2) were synthesized in the same condition, all of which were ground into powders in the glove box to isolate oxygen.

X-ray diffraction: Samples pulverized with an agate mortar were used for X-ray powder diffraction. The diffraction patterns were recorded with Cu Kα (λ = 1.5418 Å) radiation in a reflection geometry on an Inel diffractometer operating at 40 kV and 20 mA using a position-sensitive detector.

Full-range and magnified powder XRD patterns of $SnSe_{0.97-x}S_xBr_{0.03}$ and $SnSe_{0.97-x}Te_xBr_{0.03}$ (x = 0.05-0.2) are shown in **Figure S4**. All diffraction peaks for synthesized polycrystalline samples can be indexed as the orthorhombic structured SnSe. Magnified XRD patterns show that with the increasing S fractions, high angle peaks shift towards higher angles, indicating reduced unit cell volumes. On the contrary,

high angle peaks shift to lower angles with increasing Te fractions. These results are consistent with the variation of calculated lattice parameters with an increasing amount of S and Te, as shown in **Figure S5(a)** and **S5(c)**. Because the ionic radius of S^{2-} (1.84Å) is smaller than that of Se^{2-} (1.98 Å), ionic radius of Te^{2-} (2.21 Å) is larger than that of Se^{2-} (1.98 Å).

Electrical transport properties: The SPS processed pellets were cut into bars with dimensions 10 × 3 × 3 mm^3 for simultaneous measurement of the Seebeck coefficient and electrical conductivity using a Cryoall CTA instrument under a low-pressure helium atmosphere from room temperature to 800 K. The samples were coated with a thin of boron nitride (BN) to protect the instruments from the possible evaporation of samples. The uncertainty of the Seebeck coefficient and electrical conductivity measurement is within 5%.

Hall measurements: Hall coefficients (R_H) were measured under a reversible magnetic field (1.5T) by the Van der Pauw method by using a Hall measurement system (Lake Shore 8400 Series, model 8404, USA). Carrier density (n_H) was obtained by $n_H = 1/(eR_H)$.

Bandgap measurement: Room temperature optical diffuse reflectance spectra of the powder were obtained on a UV-VIS-NIR Spectrophotometer (UV-3600Plus) equipped with a polytetrafluoroethylene (PTFE) integrating sphere. The instrument is equipped with the ISR-603 integrating sphere. Samples ground into powders were spread on a plate surface compacted with $BaSO_4$ powders. In order to estimate the bandgap of samples, the reflectance versus wavelength date given in the diffuse reflectance spectra was converted to absorption date using Kubelka-Munk equations: $\alpha/S = (1 - R)^2/2R$, where R, α and S represent the reflectance, the absorption and scattering coefficients, respectively. The alloying effect was also identified through the optical absorption spectra and band gap as shown in **Figure S5(b)** and **S5(d)**.

Thermal conductivity: The SPS processed pellets were cut into coins with dimension of Ø ~ 6 mm × 1.5 mm for thermal diffusivity measurements. The thermal

diffusivities were measured with the Netzsch 457 instrument and analyzed using a Cowan model with pulse correction. To minimize the error induced by the emissivity of materials, the coins were well polished and coated with a thin layer of graphite. The thermal conductivity was calculated as $\kappa = D \cdot C_p \cdot \rho$, where D is thermal diffusivity, C_p is the specific heat capacity which was taken from reference[1] and the density (ρ) was determined using the dimensions and the mass of the sample as shown in **Table S1**. The uncertainty of the thermal conductivity is estimated to be within 8 %. Considering all the uncertainties from D, ρ and C_p, the combined uncertainty for all measurements involved in the calculation of ZT is within 20 %.

Lorenz number calculation: The Lorenz number is given by the formula:

$$L = \left(\frac{k_B}{e}\right)^2 \left(\frac{(r+7/2)F_{r+5/2}(\eta)}{(r+3/2)F_{r+1/2}(\eta)} - \left[\frac{(r+5/2)F_{r+3/2}(\eta)}{(r+3/2)F_{r+1/2}(\eta)}\right]^2\right) \qquad (S1)$$

where k_B is Boltzmann constant and η represents the reduced Fermi energy, which can be derived from the measured Seebeck coefficients *via* the following equation:

$$S = \pm \frac{k_B}{e}\left(\frac{(r+5/2)F_{r+3/2}(\eta)}{(r+3/2)F_{r+1/2}(\eta)} - \eta\right) \qquad (S2)$$

where $F_n(\eta)$ is the nth order Fermi integral:

$$F_n(\eta) = \int_0^\infty \frac{\chi^n}{1 + e^{\chi - \eta}} d\chi \qquad (S3)$$

$$\eta = \frac{E_f}{k_B T} \qquad (S4)$$

Acoustic phonon scattering is the main carrier scattering mechanism, resulting in r value of -1/2.

Scanning tunneling microscope (STM) and scanning tunneling spectroscopy (STS):

The STM experiments were performed in a commercial Unisoku system and a commercial Omicron system with base pressure below 1×10^{-10} mbar. The SnSe crystal was introduced into the UHV (ultra-high vacuum) chamber and cleaved by a

piece of sticky tape inside the vacuum chamber. O_2 (99.999 %) was deposited via a leak valve connected to a gas cylinder. During the deposition process, the substrate was held at room temperature. STM measurements were performed at 78 K. STS measurements were performed at room temperature in air and vacuum condition (around 1×10^{-10} mbar), respectively. The acquirement processes of dI/dV spectra are as follows: 1) average several individual I-V curves (around 10 curves); 2) numerical differential of the averaged I-V curves; 3) normalization by dividing averaged I-V curves.

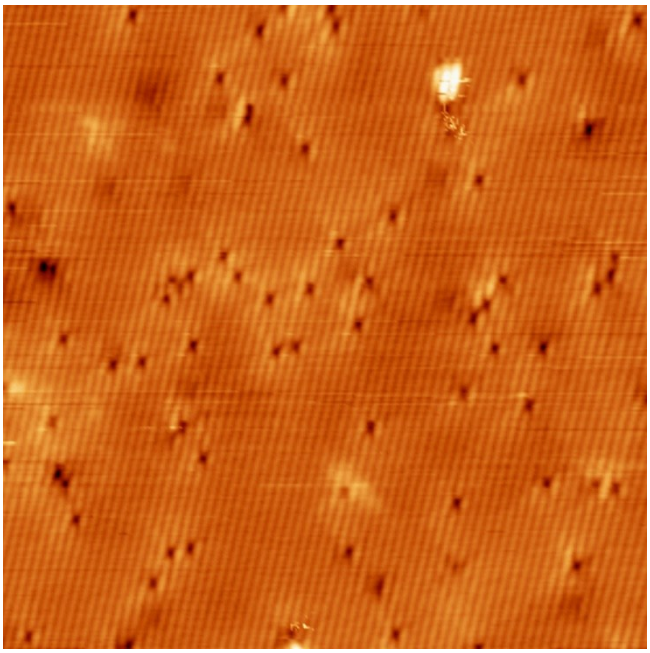

Figure S1. STM image of a fresh cleaved n-type SnSe observed at 78 K. (image size: 30 × 30 nm^2; imaging condition: $V_s = -2.0\,V$, $I_t = 20\,pA$).

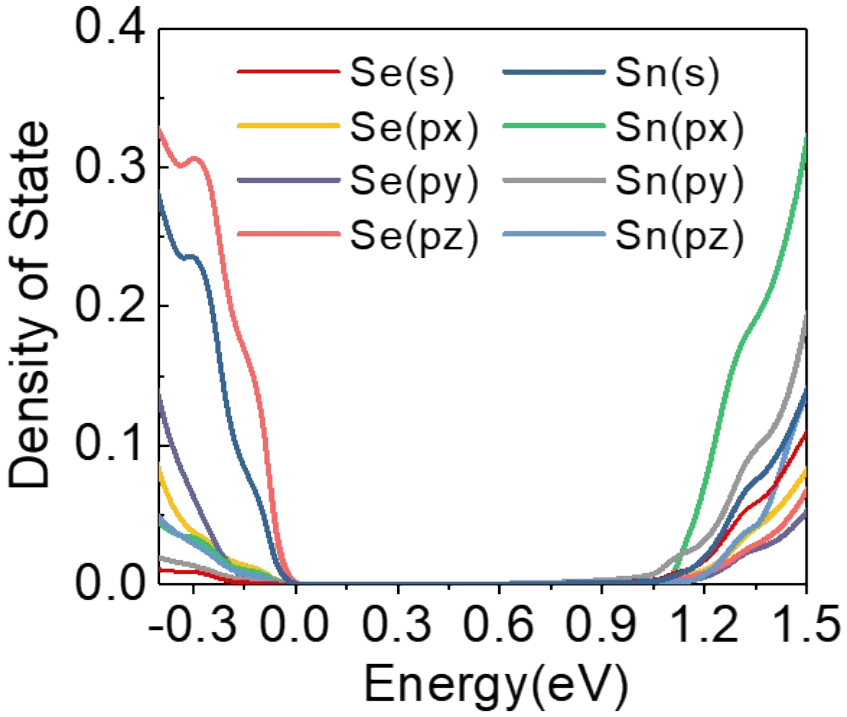

Figure S2. Calculated DOS of SnSe. The density of states (DOS) near the band edges through DFT calculations.

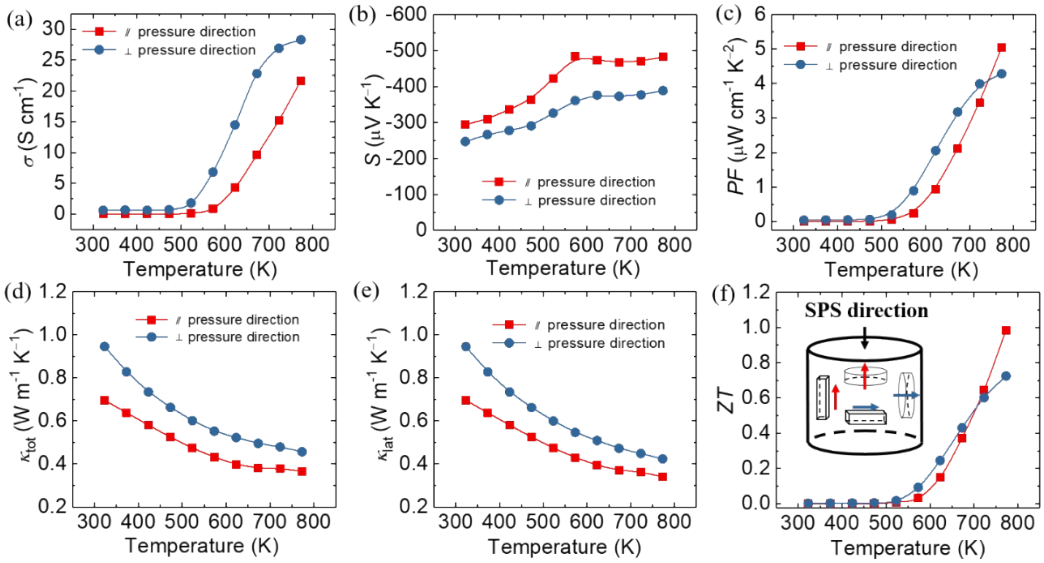

Figure S3. Thermoelectric properties of $SnSe_{0.97}Br_{0.03}$ along two directions. (a) Electrical conductivity. **(b)** Seebeck coefficient. **(c)** Power factor. **(d)** Total thermal conductivity. **(e)** Lattice thermal conductivity. **(f)** *ZT* values. Inset images: the schematic picture shows how the samples cut along the directions of perpendicular and parallel to SPS pressure direction, respectively.

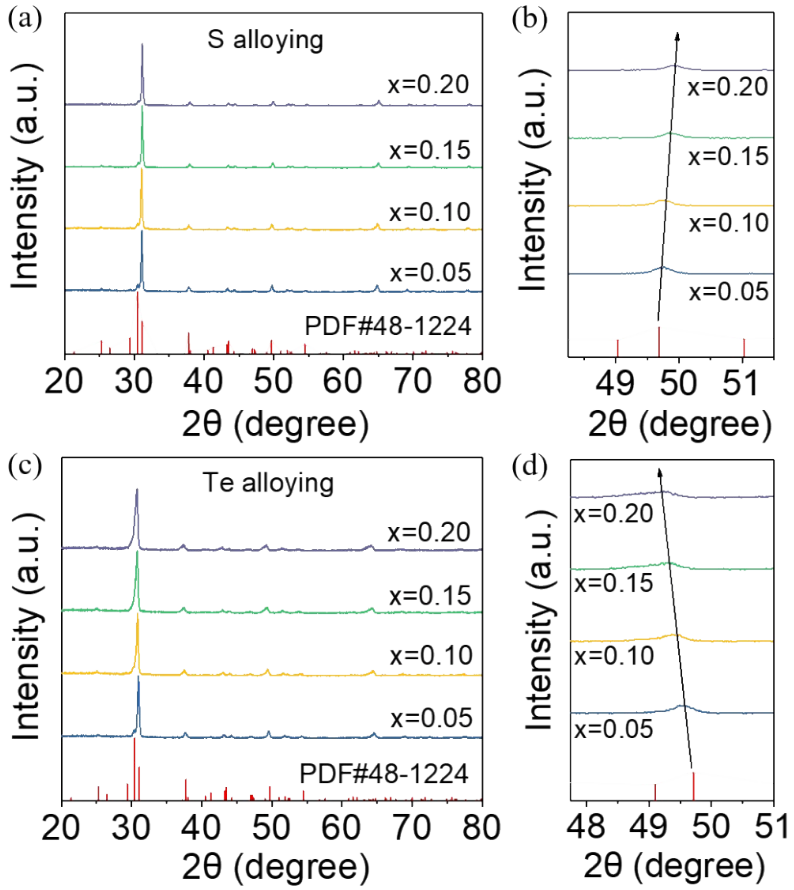

Figure S4. Full-range and enlarged powder XRD patterns. (a) Full-range and (b) Enlarged power XRD patterns for SnSe0.97-xSxBr0.03 (x=0.05, 0.1, 0.15, 0.2). (c) Full-range and (d) Enlarged power XRD patterns for SnSe0.97-xTexBr0.03 (x=0.05, 0.1, 0.15, 0.2).

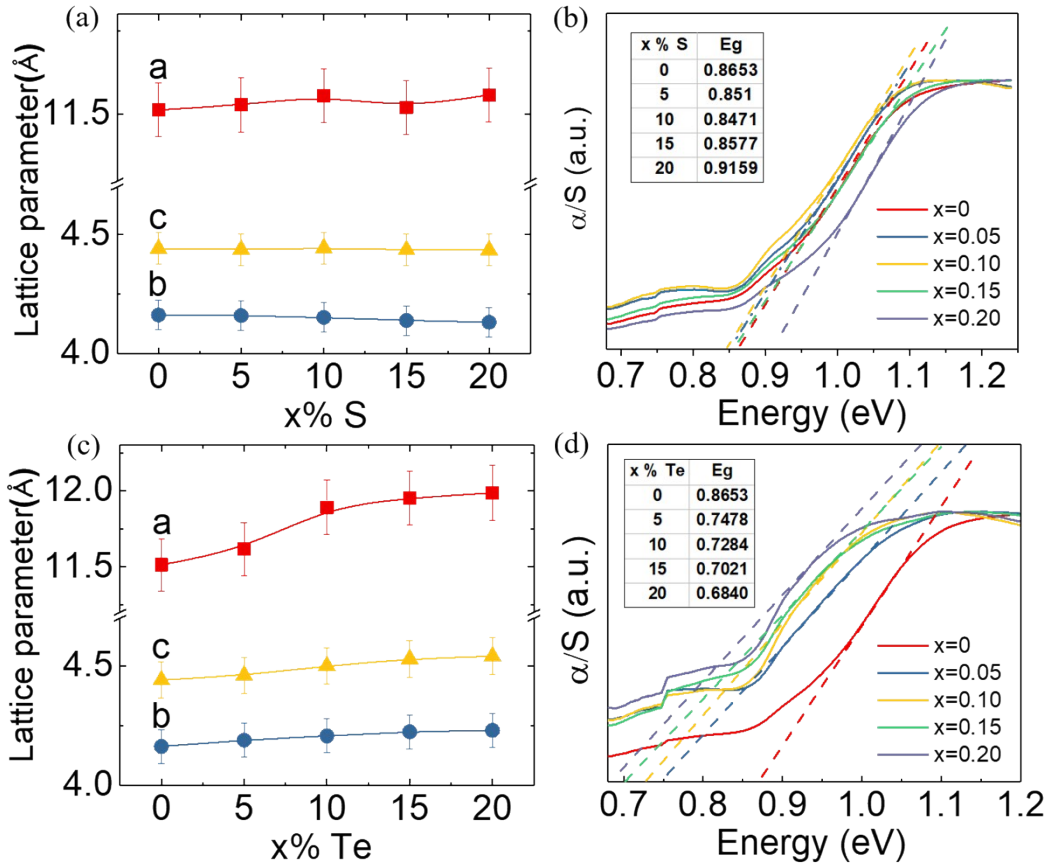

Figure S5. Lattice parameters and optical absorption spectra. (a) Lattice parameters and **(b)** Optical absorption spectra for $SnSe_{0.97-x}S_xBr_{0.03}$ (x=0.05, 0.1, 0.15, 0.2). Inset table: band gaps vary with S fractions. **(c)** Lattice parameters and **(d)** Optical absorption spectra for $SnSe_{0.97-x}Te_xBr_{0.03}$ (x=0.05, 0.1, 0.15, 0.2). Inset table: band gaps vary with Te fractions.

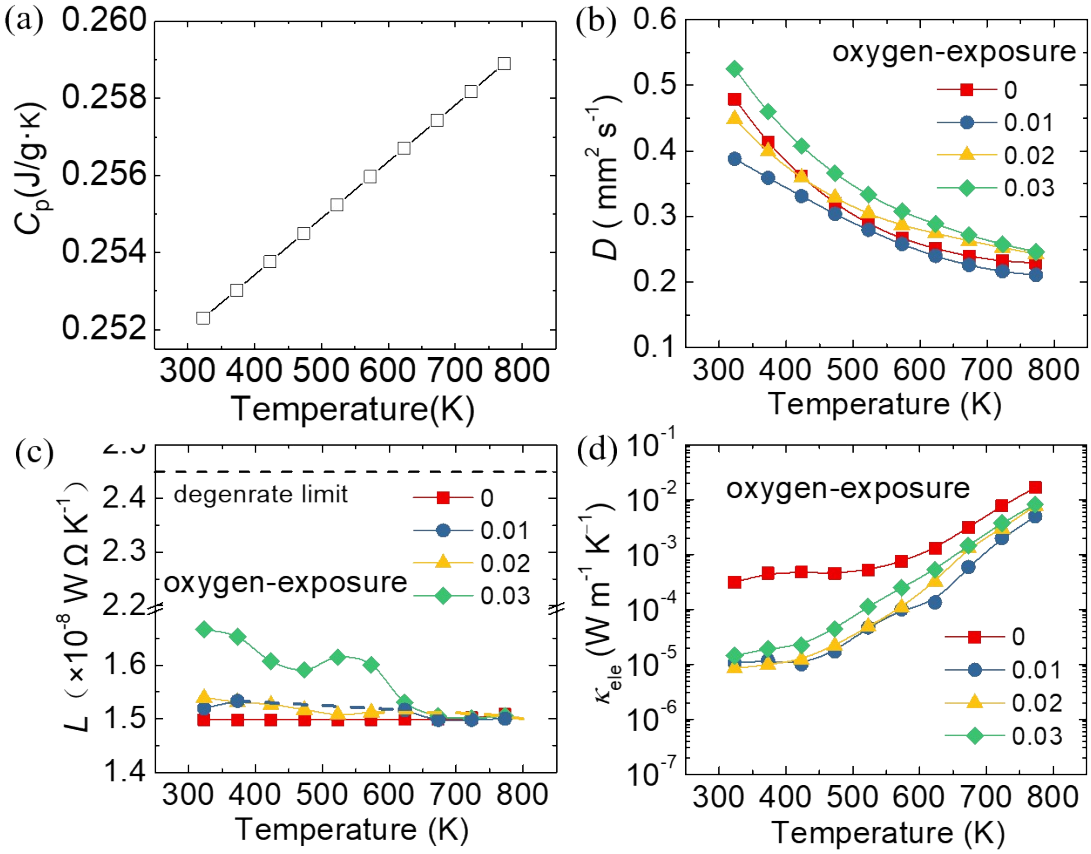

Figure S6. Thermal transport properties as a function of temperature for oxygen-exposure $SnSe_{1-x}Br_x$ (x = 0-0.03). (a) Heat capacity. **(b)** Thermal diffusivity. **(c)** Lorenz number. **(d)** Electronic thermal conductivity.

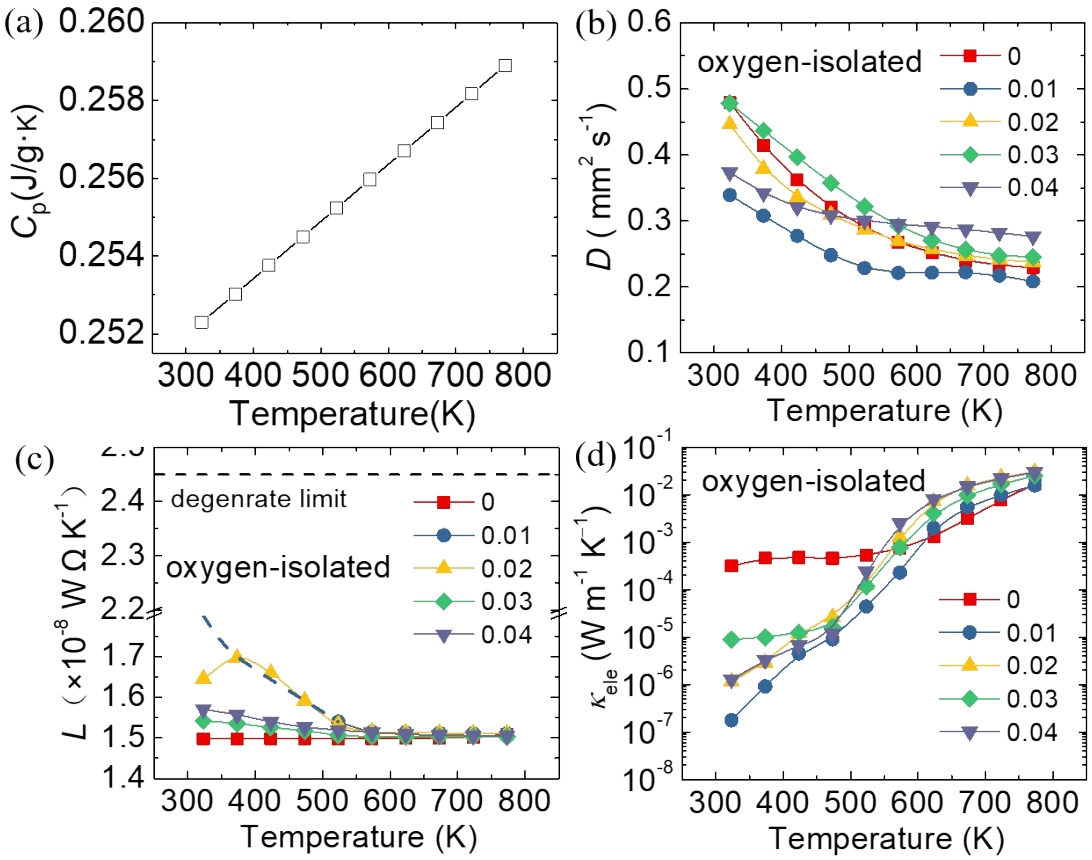

Figure S7. Thermal transport properties as a function of temperature for oxygen-isolated $SnSe_{1-x}Br_x$ (x = 0-0.04). (a) Heat capacity. **(b)** Thermal diffusivity. **(c)** Lorenz number. **(d)** Electronic thermal conductivity.

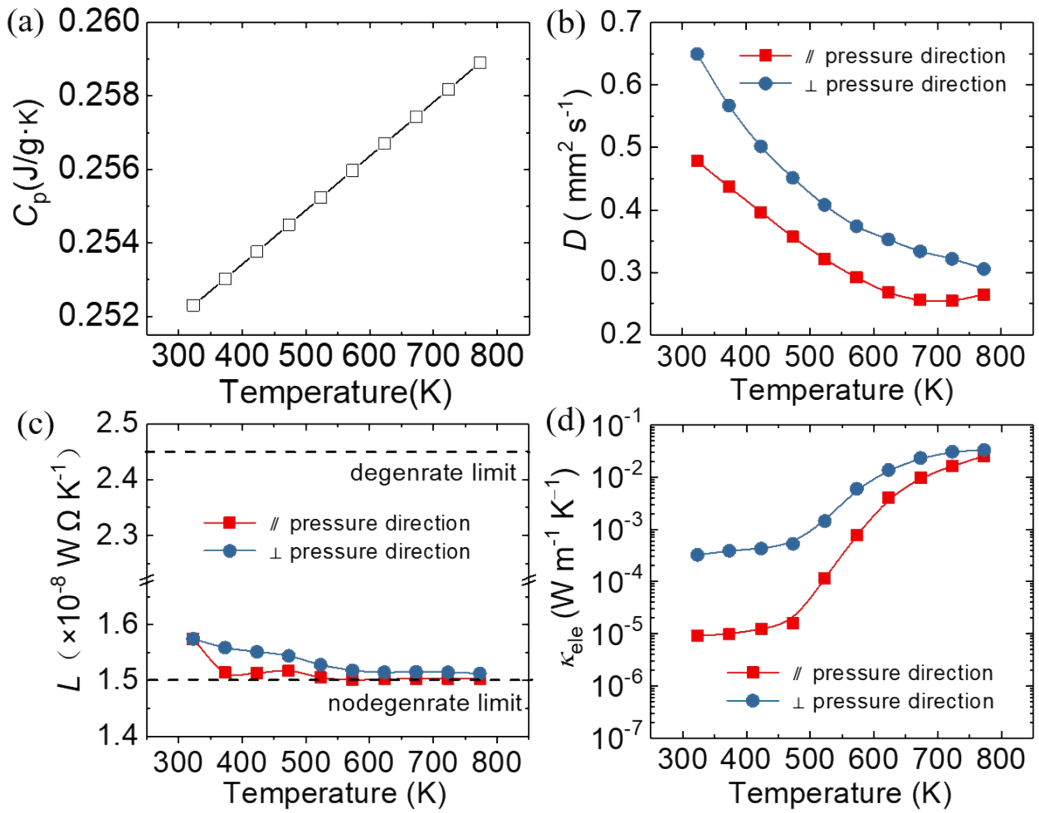

Figure S8. Thermal transport properties as a function of temperature for oxygen-isolated $SnSe_{0.97}Br_{0.03}$ along two directions. (a) Heat capacity. **(b)** Thermal diffusivity. **(c)** Lorenz number. **(d)** Electronic thermal conductivity.

Table S1. Density of samples included in this study.

$SnSe_{1-x}Br_x$ Oxygen-exposure	Density (g cm^{-3})	$SnSe_{1-x}Br_x$ Oxygen-isolated	Density (g cm^{-3})
0.01	5.82	0.01	5.85
0.02	5.80	0.02	5.86
0.03	5.74	0.03	5.77
—	—	0.04	5.83

References

1. Zhao, L. D.; Lo, S. H.; Zhang, Y. S.; Sun, H.; Tan, G. J.; Uher, C.; Wolverton, C.; Dravid, V. P.; Kanatzidis, M. G., Ultralow thermal conductivity and high thermoelectric figure of merit in SnSe crystals. *Nature* **2014,** *508* (7496), 373-377.